Tuning the Spin Density of Cobalt Single-Atom Catalysts for Efficient Oxygen Evolution

Zejun Li,[△] Zeyu Wang,[△] Shibo Xi,[△] Xiaoxu Zhao,[△] Tao Sun,[△] Jing Li, Wei Yu, Haomin Xu, Tun Seng Herng, Xiao Hai, Pin Lyu, Meng Zhao, Stephen J. Pennycook, Jun Ding, Hai Xiao,* and Jiong Lu*

ACCESS | 📊 Metrics & More | 📄 Article Recommendations | 🆂🅸 Supporting Information

ABSTRACT: Single-atom catalysts (SACs) with magnetic elements as the active center have been widely exploited for efficient electrochemical conversions. Understanding the catalytic role of spin, and thus modulating the spin density of a single-atom center, is of profound fundamental interest and technological impact. Here, we synthesized ferromagnetic single Co atom catalysts on TaS_2 monolayers (Co_1/TaS_2) as a model system to explore the spin−activity correlation for the oxygen evolution reaction (OER). A single Co atom adsorbed at the hollow site (Co_{HS}) with spin-polarized electronic states serves as the active site for OER, whose spin density can be regulated by its neighboring single Co site via tuning the Co loading. Both experimental and theoretical results reveal the spin density-dependent OER activity that an optimal spin density of Co_{HS} can be achieved with a neighboring hetero-single Co_{Ta} site (substitution of Ta by Co) for a superior OER performance, in contrast to a homo-single Co_{HS} site, which creates an excessive spin density over vicinal Co_{HS}.

Spin density engineering
Dual Co_{HS}-Co_{Ta} sites

An optimized spin density of Co_{HS} results in an optimal binding energy of oxygen species for the OER. Establishing the spin−activity correlation in SACs may create a descriptor for designing efficient magnetic SACs for renewable energy conversions.

KEYWORDS: single-atom catalysts, ferromagnetism, spin density engineering, activity descriptor, oxygen electrocatalysis
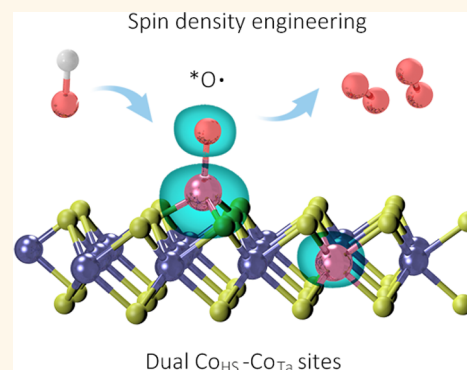
INTRODUCTION

Water splitting into hydrogen and oxygen has been one of the most promising ways to produce clean hydrogen fuel for developing sustainable energy conversion and storage technologies.[1−7] However, the oxygen evolution reaction (OER), the half-reaction of water splitting, has been the bottleneck for highly efficient hydrogen production owing to its sluggish four-electron reaction, resulting in high overpotential and low conversion efficiency.[8−11] To date, nonmagnetic noble-metal oxides (e.g., RuO_2) are generally recognized as the most effective OER catalysts.[12−14] However, the utilization of noble-metal OER catalysts is significantly stalled by their low abundance and high cost. Substantial efforts have been devoted to discovering highly active earth-abundant OER catalysts as well as to identify the general activity descriptor that governs the overall OER performance.[15−18] For example, surface oxygen binding energy, 3d electron number, and e_g electron filling of surface transition metal ions have been proposed as the activity descriptors for the rational design of efficient transition metal oxide OER catalysts.[19−24] Thus, it is vital to establish the relationship between activity and the intrinsic

properties of active sites, which can guide the design of advanced catalysts for optimized OER performance.

Apart from nonmagnetic materials, an abundance of OER catalysts containing magnetic elements also exhibit superior performance, which has recently drawn increased attention.[25−32] For instance, inverse spinel oxide $LiCoVO_4$ containing magnetically polarized channels shows excellent OER activity.[33] It is also noted that the OER performance of magnetic ferrite Ni−Fe oxides can be further enhanced under an external magnetic field, attributed to the spin-polarized surface, which favors the parallel spin alignment of oxygen atoms toward the formation of triplet oxygen molecules.[34] Although various experimental results point out the correlation between the spin character of the active sites and OER activity,[35] the detailed catalytic role of the spin state of active
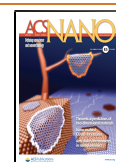
sites still remains elusive, due to the structural complexity with an unclear active site and the difficulty of synthesis of magnetic catalysts with targeted spin ordering, as well as a lack of the ability to control the spin states of active sites.

A magnetic single-metal atom anchored on a metallic support (denoted as M-SACs) offers an ideal model system for exploring the correlation between spin states of active sites and OER activity. First, M-SACs contain well-defined single-magnetic-metal active sites with local spins, which can directly bond with the oxygen intermediates.[36−39] Second, the metallic supports harbor a high density of itinerant electrons, which favor the spin ordering through the long-range spin exchange interaction between the isolated magnetic atoms *via* the Ruderman−Kittel−-Kasuya−Yosida (RKKY) mechanism.[40−42] The RKKY spin exchange between the magnetic atoms also depends on their spatial separations, whereby the spin states of single magnetic atoms can be controlled by tuning the loading of magnetic atoms. In addition, the metallic supports present high electrical conductivity, facilitating the charge transfer during electrochemical reaction.

To this end, we designed M-SACs on metallic TaS_2 monolayers with tunable loadings as a model system to explore the spin−activity correlation of OER (Figure 1). Here,
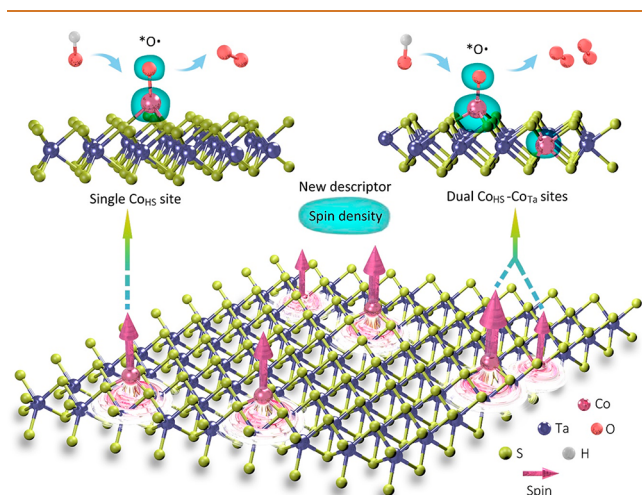

Figure 1. Schematic illustration of the spin density engineering of a single-metal active site for promoting OER within a ferromagnetic domain.

we anchored Co atoms, as a prototypical magnetic atom, on the basal plane of metallic TaS_2 monolayers through a van der Waals-space modification (VdWM) strategy established in our previous work.[43] Such a VdWM method produces two types of single Co sites on TaS_2 including the one replacing Ta atoms (Co_{Ta}) or the other bonding at the hollow site (Co_{HS}). Density functional theory (DFT) calculations reveal that the Co_{HS} act as the active sites for OER. The spin density of Co_{HS} can be regulated through the exchange interaction with the adjacent single Co sites, which is closely related to Co_{HS}−$O^{\bullet}$ binding energy. Co_{Ta} enhances the spin density over the adjacent Co_{HS} site, which results in an optimized interaction between Co_{HS} and $O^{\bullet}$ species and thus promotes OER activity. In contrast, the presence of neighboring Co_{HS} significantly increases the spin density of the Co_{HS} site, leading to a too strong binding of $O^{\bullet}$ species that hinders subsequent reactions. The DFT calculations and electrochemical measurements established a reliable link between the spin density of the active site and

OER activity, which was corroborated by the increased magnetic moment per Co atom as a function of Co loading in these ferromagnetic Co_1/TaS_2 samples. Moreover, this VdWM method can also be applied to other metal ions including as Fe^{3+}, In^{3+}, and Pd^{2+} ions, providing a general route to fabricate hetero-single-atom catalysts. Our work establishes the correlation between spin state of active sites and OER catalytic performance, which provides a descriptor associated with spin for developing efficient magnetic catalysts.

RESULTS AND DISCUSSION

Rational Design of Magnetic Single-Atom Catalysts. Co_1/TaS_2 SACs (Co_1 represents a single Co atom) with two types of single Co sites (Co_{Ta} and Co_{HS}) were prepared *via* the co-intercalation of Co^{2+} ions and tetrabutylammonium molecules into the interlayer space of metallic 2H-TaS_2 crystals,[43] according to the VdWM strategy (Figure 2a and b). The isothermal magnetization curves reveal the ferromagnetism of Co_1/TaS_2 at room temperature, suggesting the presence of a magnetic moment associated with single Co dopants, as well as their RKKY spin exchange interactions. Spin-polarized DFT calculations reveal a larger local magnetic moment of Co_{HS} as compared with the Co_{Ta} site. Therefore, Co_1/TaS_2 may provide a promising material platform to explore the spin−activity correlation by regulating the proportion and separation between Co_{HS} and Co_{Ta} sites on TaS_2.

We then designed experiments to control the proportion and distance between Co_{HS} and Co_{Ta} sites by introducing different contents of single Co atoms on TaS_2. Our theoretical calculations predict a smaller formation energy of 3.6 eV for Co_{HS}, as compared to that of Co_{Ta} (6.48 eV), suggesting a favorable formation of Co_{HS} sites during the co-intercalation process (Figure 2c). The relative ratio of the Co_{HS} and Co_{Ta} sites can be tailored due to their different formation energies. Accordingly, Co_1/TaS_2 samples with four different Co loadings were fabricated by controlling the Co^{2+} ion concentration (see Experimental Section for details). The Co loadings of Co_1/TaS_2-1, Co_1/TaS_2-2, Co_1/TaS_2-3, and Co_1/TaS_2-4 were measured to be 2.2%, 4.2%, 5.7%, and 7.3%, respectively, using inductively coupled plasma optical emission spectrometry (ICP-OES) (Table S3).

Co−S bond lengths surrounding the Co_{HS} and Co_{Ta} sites are predicted to be 2.17 and 2.38 Å, respectively (Figure 2d). Thus, the relative ratio of Co_{HS} and Co_{Ta} sites can be inferred by analyzing the averaged Co−S bond length in this series of Co_1/TaS_2 samples through the measurement of their extended X-ray absorption fine structure (EXAFS) spectra. Figure 2e shows the Fourier transform (FT) curves of the Co K-edge EXAFS spectra of Co_1/TaS_2-1, Co_1/TaS_2-2, Co_1/TaS_2-3, Co_1/TaS_2-4, and Co foil as the reference sample. All the Co_1/TaS_2 samples show no feature associated with the Co−Co bond but one dominant peak at about 1.84 Å indexed to the Co−S bond, suggesting the presence of isolated Co atoms in all the samples. Notably, an increase of Co content from Co_1/TaS_2-1 to Co_1/TaS_2-4 results in a slight shift of this dominant feature toward low-R value, indicating the average Co−S bond length becomes shorter. This suggests an increase of the proportion of Co_{HS} sites as a function of Co content due to its relatively lower formation energy.

An increase of the Co_{HS} site ratio as a function of Co loading was further validated by the Co 2p core-level X-ray photoelectron spectroscopy (XPS) measurements (Figure
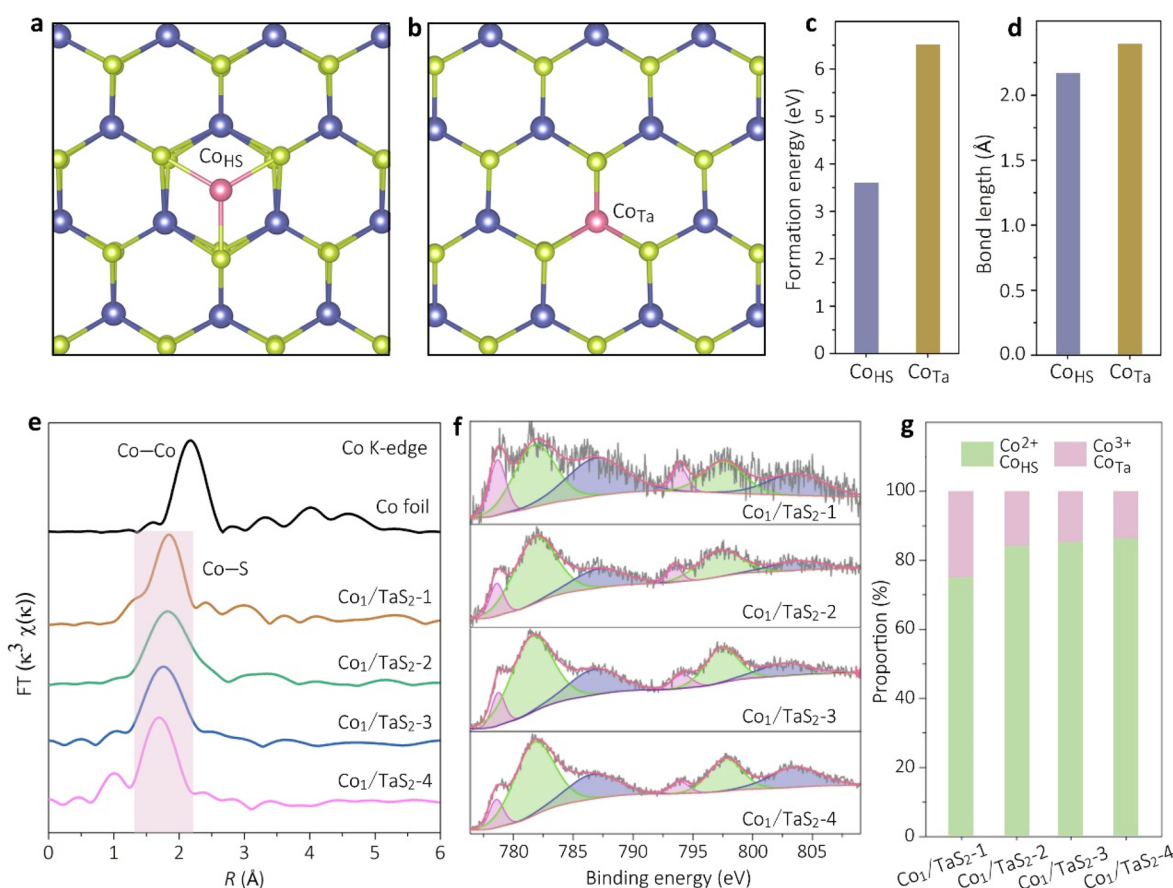
Figure 2. Magnetic single-Co-atom catalysts (Co_1/TaS_2) with a tunable density of Co_{Ta} and Co_{HS} sites. (a and b) Atomic models of Co_{HS} and Co_{Ta} sites on the basal plane of a TaS_2 lattice. (c and d) Calculated formation energy and Co−S bond length for Co_{HS} and Co_{Ta} sites. (e) Fourier transform curves of the Co K-edge EXAFS spectra of the Co_1/TaS_2 samples and Co foil. (f) XPS spectra of Co 2p for Co_1/TaS_2-1, Co_1/TaS_2-2, Co_1/TaS_2-3, and Co_1/TaS_2-4. (g) Proportional graph of the Co^{2+} (Co_{HS}) and Co^{3+} (Co_{Ta}) in the Co_1/TaS_2 samples based on the XPS analysis. The green and purple regions in (f) and (g) represent Co^{2+} and Co^{3+} components. The blue regions in (f) refer to the satellite peaks of Co^{2+} ions.

2f). All four Co_1/TaS_2 samples show two main peaks at ∼781.5 and 797.5 eV (denoted by green) ascribed to the Co $2p_{3/2}$ and Co $2p_{1/2}$ of the Co^{2+} ion, respectively.[44,45] The two adjacent satellite peaks (denoted by blue) located at higher binding energies of 786.9 and 803.2 eV are originated from the shake-up process of Co^{2+} ions in the high-spin state.[46] Furthermore, other doublet peaks (denoted by purple) at 778.7 and 793.9 eV can be ascribed to the Co^{3+} ion.[47,48] The proportion of Co^{2+} (Co^{3+}) ions in Co_1/TaS_2-1, Co_1/TaS_2-2, Co_1/TaS_2-3, and Co_1/TaS_2-4 samples is determined to be ∼74.7% (25.3%), 84.8% (15.2%), 85.6% (14.4%), and 86.6% (13.4%), respectively (Figure 2g), revealing an increase of Co^{2+} species with Co loading. Co^{2+} and Co^{3+} are likely to correspond to Co_{HS} and Co_{Ta}, respectively, since the valence state of Co_{HS} is predicted to be lower than that of Co_{Ta}. Thus, the XPS analysis also supports an increased proportion of Co_{HS} sites as a function of Co loading.

Structure Characterization of Co_1/TaS_2 Monolayers. To expose all the isolated Co sites for catalysis, we then carried out a gentle electrochemical exfoliation using quaternary ammonium cations to prepare monolayer and few-layer Co_1/TaS_2 nanosheets (see Experimental Section and Figure S1). Figure 3a and Figure S2 show the microsized as-exfoliated Co_1/TaS_2 nanosheets with varied thickness ranging from monolayers to few layers, as confirmed by the atomic force

microscopy (AFM) image (Figure 3b and Figure S3). The elemental mapping (Figure 3c) reveals a homogeneous distribution of Co, Ta, and S elements over the entire Co_1/TaS_2 flake. Co_1/TaS_2 flakes still maintain a high crystallinity of metallic $2H$-TaS_2 lattice as supported by high-resolution transmission electron microscopy (HRTEM) imaging (Figure 3d) and Raman spectroscopy (Figure S4), which facilitates the RKKY magnetic interaction and charge transfer for OER.

To trace the microscale distribution of Co_{HS} and Co_{Ta} sites on TaS_2 layers as a function of Co loadings, we performed high-angle annular dark-field scanning transmission electron microscopy (HAADF-STEM) measurements of Co_1/TaS_2 samples. Figure 3e and f present the typical HAADF-STEM images of Co_1/TaS_2-1 and Co_1/TaS_2-3 monolayers. The brightest and dim spots correspond to the Ta and S sites, while the moderately bright spots are assigned to the isolated Co atoms. The atomic sites marked by green and blue circles are Co_{Ta} and Co_{HS}, respectively. At a low Co loading, the Co_{HS} and Co_{Ta} sites are separated by a distance larger than 2 nm (Figure 3e). An increase of Co loading (Figure 3f and Figure S5) reduces the separation between adjacent Co sites, whereby the neighboring Co_{HS}-Co_{Ta} and Co_{HS}-Co_{HS} sites are formed, as illustrated in Figure 3g.

Probing the OER Activity of Co_1/TaS_2 SACs. We then evaluate the OER activity of the four Co_1/TaS_2 SACs. Linear
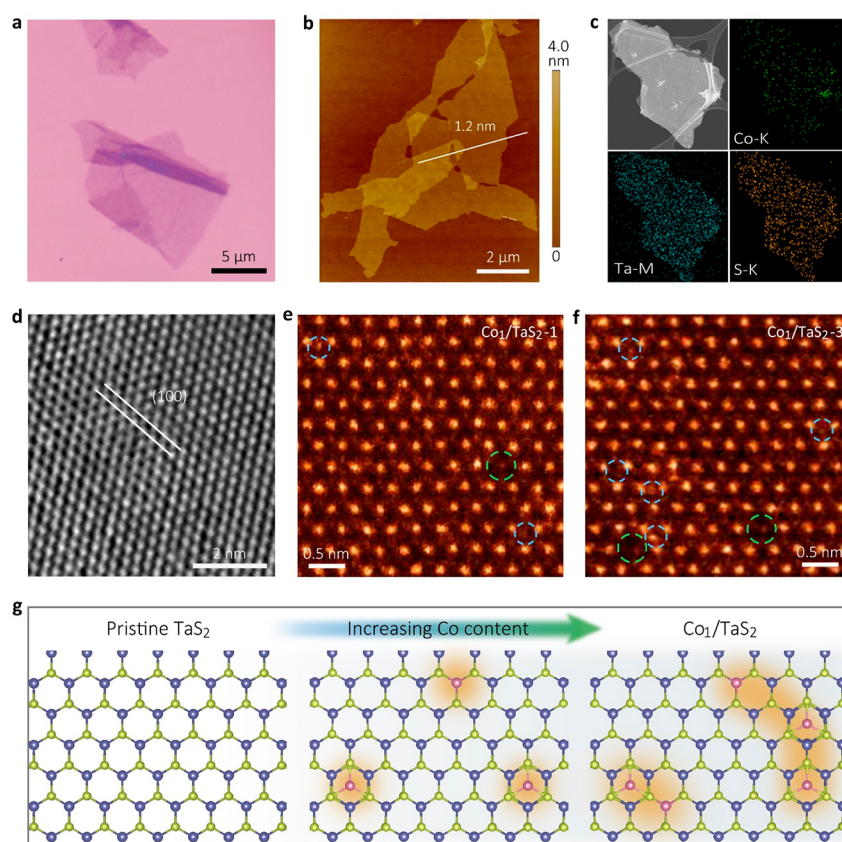
Figure 3. Characterizations of the exfoliated Co_1/TaS_2 monolayers. (a) Optical image of the typical Co_1/TaS_2 monolayers on a SiO_2/Si substrate. (b) AFM image of several exfoliated Co_1/TaS_2 monolayers, showing a thickness of about 1.2 nm. (c) EDS elemental mapping of Co-K, Ta-M, and S-K of a single Co_1/TaS_2 nanosheet. (d) Typical HRTEM image of the exfoliated Co_1/TaS_2 nanosheets showing the (100) plane of 2H-TaS_2. (e and f) HAADF-STEM images of the basal plane of a Co_1/TaS_2-1 monolayer and a Co_1/TaS_2-3 monolayer, respectively. Co_{Ta} sites and Co_{HS} sites are marked by green and blue circles, respectively. (g) Structural evolution of Co_{Ta} and Co_{HS} sites in a TaS_2 lattice as the Co loading increases.

sweep voltammetry (LSV) was carried out in a O_2-saturated 1 M KOH alkaline solution. As shown in Figure 4a, the *iR*-corrected polarization curves present an enhancement of the OER performance for Co_1/TaS_2 compared with pristine TaS_2. Interestingly, the OER activity increases with Co loadings from Co_1/TaS_2-1 to Co_1/TaS_2-3, and then it decays at a higher Co content (Co_1/TaS_2-4). At a current density of 10 mA cm^{-2} (Figure 4b), the overpotential decreases from 430 mV for pristine TaS_2 to 377, 340, and 330 mV for Co_1/TaS_2-1, $Co_1/$ TaS_2-2, and Co_1/TaS_2-3, respectively. A further increase of Co loading increases the overpotential of Co_1/TaS_2-4 to 340 mV. In addition, the current densities at 1.7 V *vs* RHE of these four samples show a similar loading-dependent trend, wherein the Co_1/TaS_2-3 shows the highest value of 77 mA cm^{-2}. Among all four Co_1/TaS_2 samples, Co_1/TaS_2-3 exhibits the lowest Tafel slope of 70 mV dec^{-1}, superior to pristine TaS_2 (145 mV dec^{-1}) and Co_1/TaS_2-4 (100 mV dec^{-1}) (Figure 4c). Therefore, the Co_1/TaS_2-3 presents the optimal OER activity with an overpotential of 330 mV at 10 mA cm^{-2} and Tafel slope of 70 mV dec^{-1}, superior to commercial RuO_2 (370 mV) OER catalysts (the OER activity of different Co_1/TaS_2 samples with various Co loadings is shown in Figure S6).

In addition, Co_1/TaS_2-3 shows a good stability throughout a 12 h test at a constant potential of 1.6 V *vs* RHE (Figure 4d). HRTEM imaging reveals that Co_1/TaS_2-3 thin flakes after the durability test still maintain a pristine 2H-TaS_2 structure

(Figure 4e). Furthermore, EXAFS spectra acquired for $Co_1/$ TaS_2-3 SACs before and after OER show very similar features, suggesting that Co atoms still maintain atomic dispersion during OER (Figure 4f). However, the major peak of $Co_1/$ TaS_2-3-OER slightly shifts to a low-*R* compared to that of the original Co_1/TaS_2-3 sample, which could be attributed to the chemical adsorption of oxygen intermediates to Co_{HS} sites during the OER process (note that the Co−O bond is shorter than that of Co−S and the major peak could be assigned to the mix of Co−S and Co−O bonds). Such a bond length variation further attests that the Co_{HS} site serves as the active center for OER. Furthermore, this VdWM method can be applied to produce various single-metal-atom-modified TaS_2 including Fe-TaS_2, In-TaS_2, and Pd-TaS_2, giving a path for designing efficient single-atom heterogeneous catalysts (see Experimental Section and Figure S7).

Theoretical Modeling of the Activity Origin of OER. To understand the origin of the excellent OER performance of Co_1/TaS_2 SACs, we performed DFT calculations to study how the Co_{HS} and Co_{Ta} influence the OER activity (Supporting Information, DFT calculations). The calculated Gibbs free energy profiles identify that the potential limiting step (PLS) for OER over the pristine TaS_2 and Co_{Ta} sites is the transformation from *O to *OOH with energy barriers of 1.60 and 1.66 eV, respectively, while the PLS over the Co_{HS} site is predicted to be the conversion from *OH to *O with a

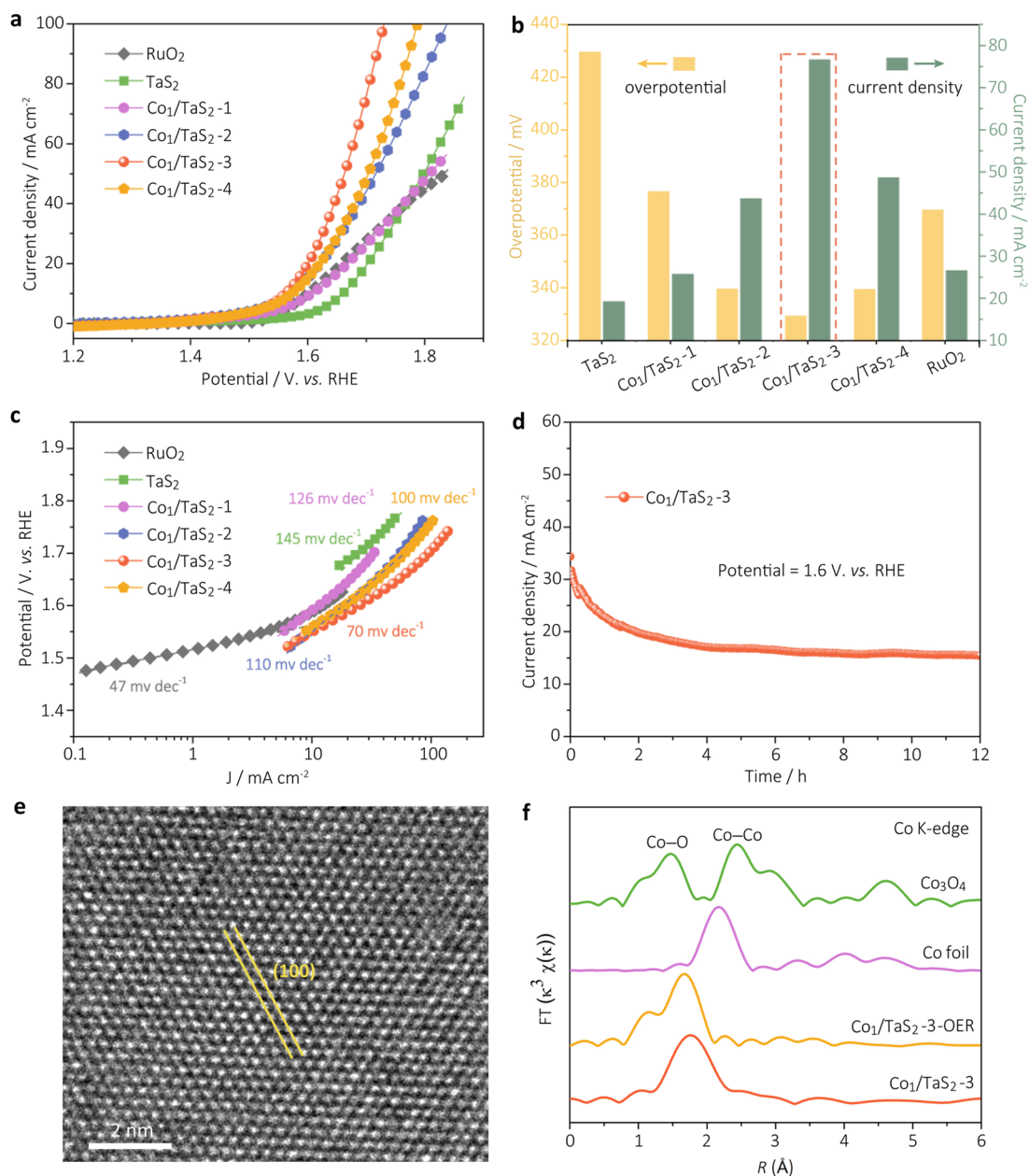**Figure 4.** Electrocatalytic OER measurements. (a) Polarization curves of pristine TaS_2 and exfoliated Co_1/TaS_2-1 to Co_1/TaS_2-4, with commercial RuO_2 for comparison. (b) Comparison of the overpotential *vs* RHE at the current density of 10 mA cm^{-2} and current density at 1.7 V *vs* RHE. (c) Tafel plots of pristine TaS_2, exfoliated Co_1/TaS_2-1 to Co_1/TaS_2-4, and RuO_2. (d) OER stability for Co_1/TaS_2-3 at 1.6 V *vs* RHE. (e) HRTEM image of the Co_1/TaS_2-3 nanosheets after the OER durability test. (f) Fourier transform curves of the Co K-edge EXAFS spectra of the Co_1/TaS_2-3 before and after OER, with Co foil and Co_3O_4 as references.

reduced energy barrier of 1.34 eV (Figure S8). Therefore, Co_{HS} sites are expected to be excellent OER active sites, compared to pristine TaS_2 and Co_{Ta} sites. Another key question is the origin of the trend of OER performance, namely, the OER activity first increases and then declines as a function of Co loading. The aforementioned STEM imaging shows that the density of the dual site including Co_{HS}-Co_{Ta} and Co_{HS}-Co_{HS} increases with an increase in Co loading, which suggests that the interaction between Co_{HS} and its vicinal Co site impacts the OER activity.

We then explored the influence of adjacent Co_{Ta} and Co_{HS} sites on the OER activity of Co_{HS} sites, which are defined as the Co_{HS}-Co_{Ta} and Co_{HS}-Co_{HS} sites, respectively (Figure S9). The calculated free energy profiles indicate that the energy

barriers for transformation from *OH to *O decrease to 0.93 and 0.49 eV over Co_{HS}-Co_{Ta} and Co_{HS}-Co_{HS} sites (Figure 5a and b), significantly lower than that over a single Co_{HS} site (1.34 eV). It is noted that the formation of *O remains as the PLS over the Co_{HS}-Co_{Ta} site, while deprotonation and desorption of *OOH become the PLS over the Co_{HS}-Co_{HS} site, leading to an increased energy barrier of about 0.96 eV. Therefore, the presence of a Co_{Ta} site near Co_{HS} at an increased loading can further decrease the energy barrier of PLS to promote the OER performance. However, when the Co loading increases above a critical value (between 5.7% and 7.4%), the presence of Co_{HS} near the single Co_{HS} or the Co_{HS}-Co_{Ta} dual site will increase the energy barrier of the PLS to reduce the OER activity (Figure 3f and g).
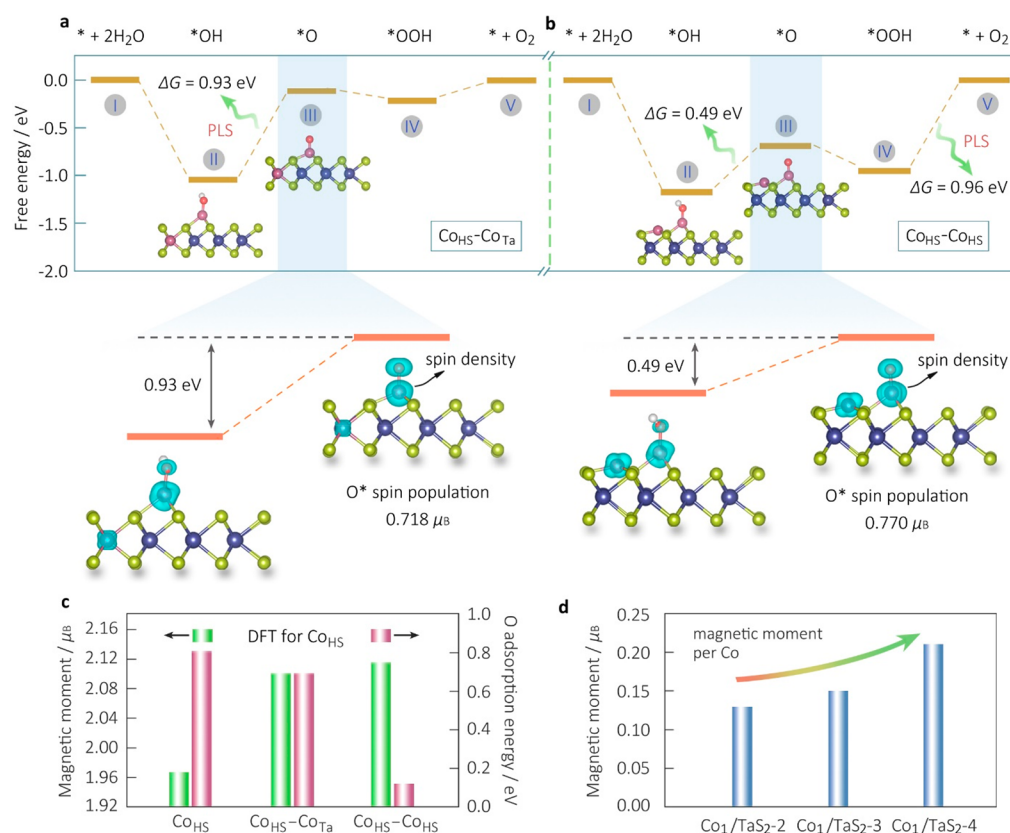
Figure 5. Theoretical study of the spin−activity correlation for OER on Co_1/TaS_2. (a and b) Free energy diagrams of OER on the Co_{HS} site with neighboring Co_{Ta} and Co_{HS} atoms. The marked and enlarged parts: the pivotal step with the transformation from *OH to *O on the Co_{HS}-Co_{Ta} and Co_{HS}-Co_{HS} sites along with spin density distributions. (c) Calculated relationship between the spin density of the Co_{HS} atom and the oxygen adsorption energy for the isolated Co_{HS}, Co_{HS}-Co_{Ta}, and Co_{HS}-Co_{HS} cases. (d) Measured magnetic moments of an individual Co atom in Co_1/TaS_2-2, Co_1/TaS_2-3, and Co_1/TaS_2-4 SAC samples.

The tunable OER activity observed here can be well described by introducing a descriptor, *i.e.*, the spin density of the Co_{HS} active site modulated by the presence of vicinal Co_{HS} and Co_{Ta} sites. The calculated spin density shows that the *O species possess a spin population of about 0.7−0.8 μ_B (Figure 5a and b, Figure S10). The nature of the active O species (*O) is identified to be an O radical forming a single bond with the surface Co_{HS} (Co_{HS}-O$^{\bullet}$). It has been predicted that the formation of a surface O radical is a key step in the OER, and a high-spin configuration of the active metal site is expected to stabilize the unpaired electron of the O radical through the exchange interactions.[49] Inspired by this prediction, we investigate the correlation between the O adsorption energy over the Co_{HS} site and the spin density of the Co_{HS} atom in the isolated Co_{HS}, Co_{HS}-Co_{Ta}, and Co_{HS}-Co_{HS} sites. As shown in Figure S11 and Figure 5c, the calculated magnetic moment of the Co_{HS} atom increases from 1.967 μ_B for the isolated Co_{HS} case to 2.100 and 2.114 μ_B for the Co_{HS}-Co_{Ta} and Co_{HS}-Co_{HS} cases, respectively (the calculations were performed at 0 K). As a result, the O adsorption energy gradually reduces from 0.8019 eV over isolated Co_{HS} to 0.6868 and 0.1119 eV over Co_{HS}-Co_{Ta} and Co_{HS}-Co_{HS} (Table S4).

Our calculations demonstrate that the neighboring Co_{Ta} enhances the spin density of the Co_{HS} active site, resulting in the formation of a more stable Co_{HS}-O$^{\bullet}$ species responsible for a better OER activity over the Co_{HS}-Co_{Ta} site, while the neighboring Co_{HS} increases the spin density of the Co_{HS} active site too much so that the Co_{HS}-O$^{\bullet}$ species becomes excessively

stable, which shifts the nature of the PLS to a higher energy barrier. Therefore, the decreased OER activity for Co_1/TaS_2-4 at the maximal loading can be ascribed to the formation of more Co_{HS}-Co_{HS} dual sites.

Furthermore, we also carried out magnetization measurements to monitor the evolution of magnetic properties for Co_1/TaS_2 samples as a function of Co loading using a commercial superconducting quantum interference device (Figures S12 and S13). According to the saturation magnetizations at 2 K (Figure 5d), the average magnetic moment of individual Co in Co_1/TaS_2-2, Co_1/TaS_2-3, and Co_1/TaS_2-4 samples is determined to be 0.13 μ_B, 0.15 μ_B, and 0.21 μ_B, respectively (note the magnetic moment of the Co_1/TaS_2-1 sample was not evaluated due to its weak ferromagnetism and unsaturated magnetization). A monotonic increase of magnetic moment per Co atom with the Co loadings can be ascribed to the spin exchange interactions between neighboring Co_{HS}-Co_{Ta} and Co_{HS}-Co_{HS} sites, which supports our theoretical prediction of the relation between the spin density of the active metal site and the OER activity. The decreased OER activity of Co_1/TaS_2-4 was presumably ascribed to the excess magnetic moment, which suppressed the catalytic activity. The best OER catalytic performance of Co_1/TaS_2-3 is likely to be attributed to the optimized spin density of active Co_{HS} sites modulated by neighboring Co_{Ta} and Co_{HS} atoms. Therefore, the spin density of an active metal site can serve as a descriptor for the OER activity.

CONCLUSIONS

In summary, we have developed a model system of ferromagnetic single-Co-atom catalysts on metallic TaS_2 monolayers to investigate the spin−activity correlation for the OER. Single Co_{HS} atoms at the hollow sites with spin-polarized states act as the active site for OER, and their spin densities can be regulated by the exchange interactions with adjacent Co sites via tuning the Co loading. The neighboring Co_{Ta} increases the spin density of the Co_{HS} active site to an optimized value, resulting in an optimal binding energy between Co_{HS} and $O^\bullet$ species and thus promoting the OER activity. The neighboring Co_{HS} overboosts the spin density of the Co_{HS} active site, leading to an excessively stable Co_{HS}-$O^\bullet$ species, which hinders the subsequent reaction and thus reduces the OER activity. This work demonstrates that a rational optimization of the spin density of single-atom active sites could effectively modulate the OER activity, which suggests the spin density may act as an activity descriptor to guide the design of efficient magnetic catalysts.

EXPERIMENTAL SECTION

Synthesis of Co_1/TaS_2 SACs with Different Co_{HS}/Co_{Ta} Ratios. 2H-TaS_2 crystals were grown through a chemical vapor transport (CVT) method using iodine (I_2) as the transport agent. A 0.05 M tetrabutylammonium chloride (TBAC) solution in dimethylforma-mide (DMF) was prepared in an ampule bottle by dissolving TBAC in DMF solvent. Then, $CoCl_2$ was added into the 0.05 M TBAC−DMF solution to form a Co−TBAC−DMF solution with different Co^{2+} concentrations (0.025, 0.02, 0.015, and 0.01 M). TaS_2 crystals were transferred into these four Co−TBAC−DMF solutions, and the air in the bottles was expelled using nitrogen gas. Subsequently, the bottles were sealed and placed in a constant-temperature oven at 110 °C for 1 week. It was found that the added Co^{2+} ions can regulate the intercalation of tetrabutylammonium molecules. A lower Co^{2+} concentration results in a larger expansion of TaS_2 layers and a higher amount of Co loading. Finally, as-synthesized Co-doped TaS_2 samples were washed with DMF and ethanol (denoted as Co_1/TaS_2-1, Co_1/TaS_2-2, Co_1/TaS_2-3, and Co_1/TaS_2-4, respectively). In addition, Fe-doped TaS_2, In-doped TaS_2, and Pd-doped TaS_2 samples were also fabricated using this method by addition of $FeCl_3$, $InCl_3$, and $PdCl_2$ salts, respectively.

Electrochemical Exfoliation of the Co_1/TaS_2 Samples. The electrochemical intercalation and expansion of Co_1/TaS_2 samples were performed using an electrochemical workstation (CHI760E) with a two-electrode system. Bulk Co_1/TaS_2 samples were placed as the working cathode, and a Pt wire was used as the counter electrode. A 0.05 M TBAC-DMF solution served as the electrolyte. A cathodic voltage of about −3 V was applied on the working electrode to drive the TBA^+ cation intercalation into the interlayer of Co_1/TaS_2, leading to a substantial expansion. The expanded Co_1/TaS_2 samples were then sonicated in DMF for further exfoliation to obtain atomically thin Co_1/TaS_2 nanosheets.

Characterizations. The optical images of exfoliated Co_1/TaS_2 nanosheets on the SiO_2/Si substrate were conducted using an Olympus BX51 microscope. The thickness of the exfoliated Co_1/TaS_2 nanosheets was characterized by atomic force microscope (Bruker Multimode 8 and DIMENSION FastScan). HRTEM and elemental composition were characterized using an FEI Titan 80-300 S/TEM. The HAADF-STEM characterization was carried out in an aberration-corrected JEOL ARM-200F system equipped with a cold field emission gun and an ASCOR probe corrector at 60 kV. XPS measurements were carried out in a custom-designed ultra-high-vacuum system with a base pressure lower than 2×10^{-10} mbar. Mg $K\alpha$ (1253.7 eV) was used as the excitation source for XPS. Raman spectroscopic measurements were performed on a WITec Alpha 300R at room temperature with a laser excitation at 532 nm. The EXAFS measurements were conducted on the XAFCA beamline of the Singapore Synchrotron Light Source (SSLS).[50] The storage ring of the SSLS was operated at 700 MeV with a beam current of 200 mA. A Si(111) double-crystal monochromator was used to filter the X-ray beam. Co foils were used for the energy calibration.

ASSOCIATED CONTENT

Ⓢ Supporting Information

The Supporting Information is available free of charge at https://pubs.acs.org/doi/10.1021/acsnano.1c00251.

DFT calculation methods (Tables S1 and S2), electro-chemical measurement methods, experimental results (Figures S1−S7, S12, and S13, Table S3), DFT calculations (Figures S8−S11, Table S4) (PDF)

AUTHOR INFORMATION

Corresponding Authors

Hai Xiao − *Department of Chemistry, Tsinghua University, Beijing 100084, China;* ⓘ orcid.org/0000-0001-9399-1584; Email: haixiao@tsinghua.edu.cn

Jiong Lu − *Department of Chemistry and Centre for Advanced 2D Materials and Graphene Research Centre, National University of Singapore, Singapore 117543, Singapore;* ⓘ orcid.org/0000-0002-3690-8235; Email: chmluj@nus.edu.sg

Authors

Zejun Li − *Department of Chemistry, National University of Singapore, Singapore 117543, Singapore;* ⓘ orcid.org/0000-0002-7582-0674

Zeyu Wang − *Department of Chemistry, Tsinghua University, Beijing 100084, China*

Shibo Xi − *Institute of Chemical and Engineering Sciences, Jurong Island 627833, Singapore*

Xiaoxu Zhao − *School of Materials Science and Engineering, Nanyang Technological University, Singapore 639798, Singapore;* ⓘ orcid.org/0000-0001-9746-3770

Tao Sun − *Department of Chemistry, National University of Singapore, Singapore 117543, Singapore*

Jing Li − *Centre for Advanced 2D Materials and Graphene Research Centre, National University of Singapore, Singapore 117546, Singapore;* ⓘ orcid.org/0000-0002-5627-4153

Wei Yu − *Department of Chemistry, National University of Singapore, Singapore 117543, Singapore;* ⓘ orcid.org/0000-0003-3468-3439

Haomin Xu − *Department of Chemistry, National University of Singapore, Singapore 117543, Singapore;* ⓘ orcid.org/0000-0003-3704-1810

Tun Seng Herng − *Department of Materials Science & Engineering, National University of Singapore, Singapore 117575, Singapore*

Xiao Hai − *Department of Chemistry, National University of Singapore, Singapore 117543, Singapore*

Pin Lyu − *Department of Chemistry, National University of Singapore, Singapore 117543, Singapore*

Meng Zhao − *Institute of Materials Research and Engineering, Agency for Science, Technology and Research (A*STAR), Singapore 138634, Singapore*

Stephen J. Pennycook − *Department of Materials Science & Engineering, National University of Singapore, Singapore 117575, Singapore*

Jun Ding − *Department of Materials Science & Engineering, National University of Singapore, Singapore 117575, Singapore;* ⓘ orcid.org/0000-0003-3752-1750

Complete contact information is available at:
https://pubs.acs.org/10.1021/acsnano.1c00251

Author Contributions

Author Contributions

△Z. Li, Z. Wang, S. Xi, X. Zhao, and T. Sun contributed equally.

Notes

ACKNOWLEDGMENTS

REFERENCES

(1) Zhu, J.; Hu, L.; Zhao, P.; Lee, L. Y. S.; Wong, K.-Y. Recent Advances in Electrocatalytic Hydrogen Evolution Using Nanoparticles. *Chem. Rev.* **2020**, *120*, 851−918.

(2) Roger, I.; Shipman, M. A.; Symes, M. D. Earth-Abundant Catalysts for Electrochemical and Photoelectrochemical Water Splitting. *Nat. Rev. Chem.* **2017**, *1*, 0003.

(3) Yao, Y.; Gu, X.-K.; He, D.; Li, Z.; Liu, W.; Xu, Q.; Yao, T.; Lin, Y.; Wang, H.-J.; Zhao, C.; Wang, X.; Yin, P.; Li, H.; Hong, X.; Wei, S.; Li, W.-X.; Li, Y.; Wu, Y. Engineering the Electronic Structure of Submonolayer Pt on Intermetallic Pd_3Pb *via* Charge Transfer Boosts the Hydrogen Evolution Reaction. *J. Am. Chem. Soc.* **2019**, *141*, 19964−19968.

(4) Lu, Q.; Yu, Y.; Ma, Q.; Chen, B.; Zhang, H. 2D Transition-Metal-Dichalcogenide-Nanosheet-Based Composites for Photocatalytic and Electrocatalytic Hydrogen Evolution Reactions. *Adv. Mater.* **2016**, *28*, 1917−1933.

(5) Lu, X. F.; Yu, L.; Lou, X. W. Highly Crystalline Ni-Doped FeP/Carbon Hollow Nanorods as All-PH Efficient and Durable Hydrogen Evolving Electrocatalysts. *Sci. Adv.* **2019**, *5*, No. eaav6009.

(6) Yang, J.; Mohmad, A. R.; Wang, Y.; Fullon, R.; Song, X.; Zhao, F.; Bozkurt, I.; Augustin, M.; Santos, E. J. G.; Shin, H. S.; Zhang, W.; Voiry, D.; Jeong, H. Y.; Chhowalla, M. Ultrahigh-Current-Density Niobium Disulfide Catalysts for Hydrogen Evolution. *Nat. Mater.* **2019**, *18*, 1309−131.

(7) Zhang, Z.; Cui, Z.-H.; Jimenez-Izal, E.; Sautet, P.; Alexandrova, A. N. Hydrogen Evolution on Restructured B-Rich WB: Metastable Surface States and Isolated Active Sites. *ACS Catal.* **2020**, *10*, 13867−13877.

(8) Jiao, Y.; Zheng, Y.; Jaroniec, M.; Qiao, S. Z. Design of Electrocatalysts for Oxygen- and Hydrogen-Involving Energy Conversion Reactions. *Chem. Soc. Rev.* **2015**, *44*, 2060−2086.

(9) Wu, Z.-P.; Lu, X. F.; Zang, S.-Q.; Lou, X. W. Non-Noble-Metal-Based Electrocatalysts toward the Oxygen Evolution Reaction. *Adv. Funct. Mater.* **2020**, *30*, 1910274.

(10) Xie, J.; Zhang, X.; Zhang, H.; Zhang, J.; Li, S.; Wang, R.; Pan, B.; Xie, Y. Intralayered Ostwald Ripening to Ultrathin Nanomesh Catalyst with Robust Oxygen-Evolving Performance. *Adv. Mater.* **2017**, *29*, 1604765.

(11) Xu, K.; Ding, H.; Lv, H.; Chen, P.; Lu, X.; Cheng, H.; Zhou, T.; Liu, S.; Wu, X.; Wu, C.; Xie, Y. Dual Electrical-Behavior Regulation on Electrocatalysts Realizing Enhanced Electrochemical Water Oxidation. *Adv. Mater.* **2016**, *28*, 3326−3332.

(12) Rao, R. R.; Kolb, M. J.; Giordano, L.; Pedersen, A. F.; Katayama, Y.; Hwang, J.; Mehta, A.; You, H.; Lunger, J. R.; Zhou, H.; Halck, N. B.; Vegge, T.; Chorkendorff, I.; Stephens, I. E. L.; Shao-Horn, Y. Operando Identification of Site-Dependent Water Oxidation Activity on Ruthenium Dioxide Single-Crystal Surfaces. *Nat. Catal.* **2020**, *3*, 516−525.

(13) Lee, Y.; Suntivich, J.; May, K. J.; Perry, E. E.; Shao-Horn, Y. Synthesis and Activities of Rutile IrO_2 and RuO_2 Nanoparticles for Oxygen Evolution in Acid and Alkaline Solutions. *J. Phys. Chem. Lett.* **2012**, *3*, 399−404.

(14) Park, S.; Shao, Y.; Liu, J.; Wang, Y. Oxygen Electrocatalysts for Water Electrolyzers and Reversible Fuel Cells: Status and Perspective. *Energy Environ. Sci.* **2012**, *5*, 9331−9344.

(15) Hunter, B. M.; Gray, H. B.; Müller, A. M. Earth-Abundant Heterogeneous Water Oxidation Catalysts. *Chem. Rev.* **2016**, *116*, 14120−14136.

(16) Chen, P.; Tong, Y.; Wu, C.; Xie, Y. Surface/Interfacial Engineering of Inorganic Low-Dimensional Electrode Materials for Electrocatalysis. *Acc. Chem. Res.* **2018**, *51*, 2857−2866.

(17) Yang, Z.; Zhao, C.; Qu, Y.; Zhou, H.; Zhou, F.; Wang, J.; Wu, Y.; Li, Y. Trifunctional Self-Supporting Cobalt-Embedded Carbon Nanotube Films for ORR, OER, and HER Triggered by Solid Diffusion from Bulk Metal. *Adv. Mater.* **2019**, *31*, 1808043.

(18) Yang, B.; Burch, R.; Hardacre, C.; Headdock, G.; Hu, P. Understanding the Optimal Adsorption Energies for Catalyst Screening in Heterogeneous Catalysis. *ACS Catal.* **2014**, *4*, 182−186.

(19) Rossmeisl, J.; Qu, Z. W.; Zhu, H.; Kroes, G. J.; Nørskov, J. K. Electrolysis of Water on Oxide Surfaces. *J. Electroanal. Chem.* **2007**, *607*, 83−89.

(20) Man, I. C.; Su, H.-Y.; Calle-Vallejo, F.; Hansen, H. A.; Martínez, J. I.; Inoglu, N. G.; Kitchin, J.; Jaramillo, T. F.; Nørskov, J. K.; Rossmeisl, J. Universality in Oxygen Evolution Electrocatalysis on Oxide Surfaces. *ChemCatChem* **2011**, *3*, 1159−1165.

(21) Bockris, J. O. M.; Otagawa, T. The Electrocatalysis of Oxygen Evolution on Perovskites. *J. Electrochem. Soc.* **1984**, *131*, 290−302.

(22) Suntivich, J.; May, K. J.; Gasteiger, H. A.; Goodenough, J. B.; Shao-Horn, Y. A Perovskite Oxide Optimized for Oxygen Evolution Catalysis from Molecular Orbital Principles. *Science* **2011**, *334*, 1383.

(23) Hwang, J.; Rao, R. R.; Giordano, L.; Katayama, Y.; Yu, Y.; Shao-Horn, Y. Perovskites in Catalysis and Electrocatalysis. *Science* **2017**, *358*, 751.

(24) Ouyang, T.; Wang, X.-T.; Mai, X.-Q.; Chen, A.-N.; Tang, Z.-Y.; Liu, Z.-Q. Coupling Magnetic Single-Crystal $Co_2Mo_3O_8$ with Ultrathin Nitrogen-Rich Carbon Layer for Oxygen Evolution Reaction. *Angew. Chem., Int. Ed.* **2020**, *59*, 11948−11957.

(25) Shen, G.; Zhang, R.; Pan, L.; Hou, F.; Zhao, Y.; Shen, Z.; Mi, W.; Shi, C.; Wang, Q.; Zhang, X.; Zou, J.-J. Regulating the Spin State of Fe^{III} by Atomically Anchoring on Ultrathin Titanium Dioxide for Efficient Oxygen Evolution Electrocatalysis. *Angew. Chem., Int. Ed.* **2020**, *59*, 2313−2317.

(26) Chen, P.; Zhou, T.; Xing, L.; Xu, K.; Tong, Y.; Xie, H.; Zhang, L.; Yan, W.; Chu, W.; Wu, C.; Xie, Y. Atomically Dispersed Iron-Nitrogen Species as Electrocatalysts for Bifunctional Oxygen Evolution and Reduction Reactions. *Angew. Chem., Int. Ed.* **2017**, *56*, 610−614.

(27) Liu, H.; He, Q.; Jiang, H.; Lin, Y.; Zhang, Y.; Habib, M.; Chen, S.; Song, L. Electronic Structure Reconfiguration toward Pyrite NiS_2 *via* Engineered Heteroatom Defect Boosting Overall Water Splitting. *ACS Nano* **2017**, *11*, 11574−11583.

(28) Xiong, Q.; Wang, Y.; Liu, P.-F.; Zheng, L.-R.; Wang, G.; Yang, H.-G.; Wong, P.-K.; Zhang, H.; Zhao, H. Cobalt Covalent Doping in

MoS$_2$ to Induce Bifunctionality of Overall Water Splitting. *Adv. Mater.* **2018**, *30*, 1801450.

(29) Han, X.; Ling, X.; Yu, D.; Xie, D.; Li, L.; Peng, S.; Zhong, C.; Zhao, N.; Deng, Y.; Hu, W. Atomically Dispersed Binary Co-Ni Sites in Nitrogen-Doped Hollow Carbon Nanocubes for Reversible Oxygen Reduction and Evolution. *Adv. Mater.* **2019**, *31*, 1905622.

(30) Dai, L.; Chen, Z.-N.; Li, L.; Yin, P.; Liu, Z.; Zhang, H. Ultrathin Ni(0)-Embedded Ni(OH)$_2$ Heterostructured Nanosheets with Enhanced Electrochemical Overall Water Splitting. *Adv. Mater.* **2020**, *32*, 1906915.

(31) Cheng, W.; Lu, X. F.; Luan, D.; Lou, X. W. NiMn-Based Bimetal-Organic Framework Nanosheets Supported on Multi-Channel Carbon Fibers for Efficient Oxygen Electrocatalysis. *Angew. Chem., Int. Ed.* **2020**, *59*, 18234−18239.

(32) Wang, J.; Wu, H.; Gao, D.; Miao, S.; Wang, G.; Bao, X. High-Density Iron Nanoparticles Encapsulated within Nitrogen-Doped Carbon Nanoshell as Efficient Oxygen Electrocatalyst for Zinc-Air Battery. *Nano Energy* **2015**, *13*, 387−396.

(33) Chen, R. R.; Sun, Y.; Ong, S. J. H.; Xi, S.; Du, Y.; Liu, C.; Lev, O.; Xu, Z. J. Antiferromagnetic Inverse Spinel Oxide LiCoVO$_4$ with Spin-Polarized Channels for Water Oxidation. *Adv. Mater.* **2020**, *32*, 1907976.

(34) Garcés-Pineda, F. A.; Blasco-Ahicart, M.; Nieto-Castro, D.; López, N.; Galán-Mascarós, J. R. Direct Magnetic Enhancement of Electrocatalytic Water Oxidation in Alkaline Media. *Nat. Energy* **2019**, *4*, 519−525.

(35) Sun, Y.; Sun, S.; Yang, H.; Xi, S.; Gracia, J.; Xu, Z. J. Spin-Related Electron Transfer and Orbital Interactions in Oxygen Electrocatalysis. *Adv. Mater.* **2020**, *32*, 2003297.

(36) Zhao, D.; Zhuang, Z.; Cao, X.; Zhang, C.; Peng, Q.; Chen, C.; Li, Y. Atomic Site Electrocatalysts for Water Splitting, Oxygen Reduction and Selective Oxidation. *Chem. Soc. Rev.* **2020**, *49*, 2215−2264.

(37) Kaiser, S. K.; Chen, Z.; Faust Akl, D.; Mitchell, S.; Pérez-Ramírez, J. Single-Atom Catalysts across the Periodic Table. *Chem. Rev.* **2020**, *120*, 11703−11809.

(38) Qu, Y.; Wang, L.; Li, Z.; Li, P.; Zhang, Q.; Lin, Y.; Zhou, F.; Wang, H.; Yang, Z.; Hu, Y.; Zhu, M.; Zhao, X.; Han, X.; Wang, C.; Xu, Q.; Gu, L.; Luo, J.; Zheng, L.; Wu, Y. Ambient Synthesis of Single-Atom Catalysts from Bulk Metal *via* Trapping of Atoms by Surface Dangling Bonds. *Adv. Mater.* **2019**, *31*, 1904496.

(39) Kaiser, S. K.; Fako, E.; Manzocchi, G.; Krumeich, F.; Hauert, R.; Clark, A. H.; Safonova, O. V.; López, N.; Pérez-Ramírez, J. Nanostructuring Unlocks High Performance of Platinum Single-Atom Catalysts for Stable Vinyl Chloride Production. *Nat. Catal.* **2020**, *3*, 376−385.

(40) Aristov, D. N. Indirect RKKY Interaction in Any Dimensionality. *Phys. Rev. B: Condens. Matter Mater. Phys.* **1997**, *55*, 8064−8066.

(41) Yosida, K. Magnetic Properties of Cu-Mn Alloys. *Phys. Rev.* **1957**, *106*, 893−898.

(42) Fukuma, Y.; Asada, H.; Miyawaki, S.; Koyanagi, T.; Senba, S.; Goto, K.; Sato, H. Carrier-Induced Ferromagnetism in Ge$_{0.92}$Mn$_{0.08}$Te Epilayers with a Curie Temperature up to 190 K. *Appl. Phys. Lett.* **2008**, *93*, 252502.

(43) Li, Z.; Zhang, X.; Zhao, X.; Li, J.; Herng, T. S.; Xu, H.; Lin, F.; Lyu, P.; Peng, X.; Yu, W.; Hai, X.; Chen, C.; Yang, H.; Martin, J.; Lu, J.; Luo, X.; Castro Neto, A. H.; Pennycook, S. J.; Ding, J.; Feng, Y.; et al. Imprinting Ferromagnetism and Superconductivity in Single Atomic Layers of Molecular Superlattices. *Adv. Mater.* **2020**, *32*, 1907645.

(44) Sennu, P.; Christy, M.; Aravindan, V.; Lee, Y.-G.; Nahm, K. S.; Lee, Y.-S. Two-Dimensional Mesoporous Cobalt Sulfide Nanosheets as a Superior Anode for a Li-Ion Battery and a Bifunctional Electrocatalyst for the Li-O$_2$ System. *Chem. Mater.* **2015**, *27*, 5726−5735.

(45) Li, W.; Gao, X.; Xiong, D.; Wei, F.; Song, W.-G.; Xu, J.; Liu, L. Hydrothermal Synthesis of Monolithic Co$_3$Se$_4$ Nanowire Electrodes for Oxygen Evolution and Overall Water Splitting with High Efficiency and Extraordinary Catalytic Stability. *Adv. Energy Mater.* **2017**, *7*, 1602579.

(46) Wu, H.-X.; Zhang, C.-X.; Jin, L.; Yang, H.; Yang, S.-P. Preparation and Magnetic Properties of Cobalt Nanoparticles with Dendrimers as Templates. *Mater. Chem. Phys.* **2010**, *121*, 342−348.

(47) Zhu, H.; Zhang, J.; Yanzhang, R.; Du, M.; Wang, Q.; Gao, G.; Wu, J.; Wu, G.; Zhang, M.; Liu, B.; Yao, J.; Zhang, X. When Cubic Cobalt Sulfide Meets Layered Molybdenum Disulfide: A Core-Shell System toward Synergetic Electrocatalytic Water Splitting. *Adv. Mater.* **2015**, *27*, 4752−4759.

(48) Liu, Q.; Zhang, J.; Liu, Q.; Zhang, J. A General and Controllable Synthesis of Co$_m$S$_n$ (Co$_9$S$_8$, Co$_3$S$_4$, and Co$_{1-x}$S) Hierarchical Microspheres with Homogeneous Phases. *CrystEngComm* **2013**, *15*, 5087−5092.

(49) Xiao, H.; Shin, H.; Goddard, W. A. Synergy between Fe and Ni in the Optimal Performance of (Ni,Fe)OOH Catalysts for the Oxygen Evolution Reaction. Proc. *Proc. Natl. Acad. Sci. U. S. A.* **2018**, *115*, 5872.

(50) Du, Y.; Zhu, Y.; Xi, S.; Yang, P.; Moser, H. O.; Breese, M. B. H.; Borgna, A. XAFCA: A New XAFS Beamline for Catalysis Research. *J. Synchrotron Radiat.* **2015**, *22*, 839−843.